

# Design and Operation of a MEMS-Based Material Testing System for Nanomechanical Characterization

Horacio D. Espinosa, Yong Zhu, and Nicolaie Moldovan

**Abstract**—*In situ* mechanical characterization of nanostructures, such as carbon nanotubes and metallic nanowires, in scanning and transmission electron microscopes is essential for the understanding of material behavior at the nanoscale. This paper describes the design, fabrication, and operation of a novel microelectromechanical-systems (MEMS)-based material testing system used for *in situ* tensile testing of nanostructures. The device consists of an actuator and a load sensor with a specimen in between. Two types of actuators, in-plane thermal and comb drive actuators, are used to pull the specimens in displacement control and force control modes, respectively. The load sensor works based on differential capacitive sensing, from which the sensor displacement is recorded. By determining sensor stiffness from mechanical resonance measurements, the load on the specimen is obtained. Load sensors with different stiffness were fabricated. The best resolutions were achieved with load sensors that are designed for testing nanotubes, reaching 0.05 fF in capacitance, 1 nm in displacement, and 12 nN in load. For the first time, this MEMS-based material testing scheme offers the possibility of continuous observation of the specimen deformation and fracture with subnanometer resolution, while simultaneously measuring the applied load electronically with nano-Newton resolution. The overall device performance is demonstrated by testing free-standing cofabricated polysilicon films and multiwalled carbon nanotubes. [1670]

**Index Terms**—Capacitive sensing, carbon nanotubes, *in situ* microscopy, load sensor, nanomechanics, nanostructure, nanowires.

## I. INTRODUCTION

A VARIETY of nanostructures, including carbon nanotubes and nanowires, have stimulated extensive research activities in science and technology. Due to their excellent properties such as small size, low density, and high strength, they have been used in broad applications ranging from nanocomposites to nanoelectromechanical system (NEMS) [1]. These applications require an accurate evaluation of the mechanical properties of the nanostructures.

A number of experimental techniques that are dedicated to this purpose include thermally- or electrostatically- induced

vibration inside a transmission electron microscope (TEM) [2], lateral bending that is induced by atomic force microscope (AFM) probes [3], and tensile testing *in situ* scanning electron microscopes (SEM) [4]. A general shortcoming of these techniques is that they do not possess a well-controlled load application mechanism and do not permit simultaneous and independent load-deformation measurements at the nanoscale. Hence, there is an increasing need to develop novel nanoscale material testing systems that possess superior resolution and accuracy.

Microelectromechanical systems (MEMS) offer the potential of providing such a material testing system. While MEMS consist of micrometer-scale components, they have the capability of achieving nanometer displacement resolution and femto-Newton load resolution. In this context, both electrostatic [5] and thermal actuators [6]–[9] were demonstrated as possible actuators. In particular, MEMS actuators have been successfully used in on-chip testing of mechanical properties of MEMS materials [10], [11]. With the aid of compliant mechanisms [12], [13], large displacement ranges (10–20  $\mu\text{m}$ ) have been achieved. However, those devices were not able to directly measure the load by a load sensor. Following a different approach, Haque and Saif [14] developed a microfabricated Si single crystal rig to test thin films inside SEM and TEM. An external piezo-actuator was used to pull the specimen, and a flexible beam was used as a load sensor. However, both displacements had to be measured using electron beam imaging. As a result, this setup is not capable of simultaneously measuring both load and deformation at high magnification because a shift of the electron beam is needed.

Here, we report the development of a MEMS stage for the *in situ* tensile, compressive, and indentation testing of nanostructures using an alternative approach, which is to electronically measure the load [15]. This scheme offers the possibility of continuous observation of the specimen deformation and failure at high magnification, while simultaneously measuring/recording the applied load. Due to its small size, the MEMS device can easily be placed inside a SEM chamber and a TEM holder [16]. It can also be employed to perform *in situ* testing in scanning probe microscopes and synchrotron X-ray nanodiffraction stages.

This paper is organized as follows. Section II discusses the various design aspects and fabrication of the device. Section III describes the device characterization and calibration. *In situ* SEM testing of cofabricated freestanding polysilicon films and *in situ* TEM testing of multiwalled carbon nanotubes (MWCNTs) are reported in Section IV to illustrate the device performance.

Manuscript received August 8, 2005; revised September 10, 2006. This work was supported by the National Science Foundation under Award DMR-0315561. Nanomanipulation and *in situ* TEM testing were carried out at the Center for Microanalysis of Materials, University of Illinois, which is partially supported by the U.S. Department of Energy under Grant DEFG02-96-ER45439. Subject Editor S. M. Spearing.

The authors are with the Department of Mechanical Engineering, Northwestern University, Evanston, IL 60208-3111 USA (e-mail: espinosa@northwestern.edu).

Color versions of one or more of the figures in this paper are available online at <http://ieeexplore.ieee.org>.

Digital Object Identifier 10.1109/JMEMS.2007.905739

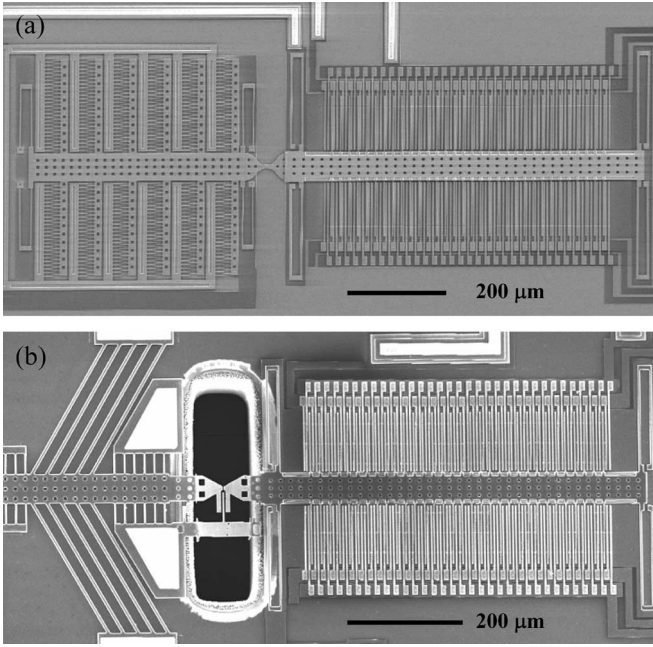


Fig. 1. Two types of MEMS-based material testing systems used for *in situ* mechanical testing of nanostructures, including (a) comb drive actuator and (b) thermal actuator.

## II. MEMS-BASED TESTING STAGE: DESIGN AND FABRICATION

The MEMS device that we developed consists of an actuator and a load sensor, with a specimen in between (Fig. 1). Two types of actuators, electrostatic (comb drive) and thermal actuators, have been employed. The comb drive actuator is force controlled and suitable in testing relatively compliant specimens (e.g., nanotubes). The thermal actuator is displacement controlled, which is very useful in testing relatively stiff and brittle samples (e.g., nanowires and ultrathin films). The load sensor is based on differential capacitive sensing, which has been successfully used in accelerometers (Analog Devices, Norwood, MA). The load sensor measures the load that is electrically applied to the specimen rather than by electron microscopy imaging, which was the case for some previous mechanical testing methods [4]. Microscopy can thus be dedicated to the observation of local specimen deformations with up to a subnanometer resolution. A large variety of materials can be investigated using this device, including thin films, 1-D nanostructures (e.g., nanotubes and nanowires), and biological molecules (e.g., proteins and DNAs). As we will explain in the subsequent sections, the stiffness of the actuator and load sensor needs to be tailored for the specimen being investigated. In this paper, thin-film specimens were cofabricated during the device microfabrication process, while nanostructures were mounted across a gap between the actuator and the load sensor using a nanomanipulator [5], [15].

### A. Actuator

Electrostatic comb drive actuators and electrothermal actuators (ETAs) were adopted due to their good compatibility with surface micromachining. Their details and functioning

principles are well described in the literature. In this paper, we primarily report the design and characterization of ETAs. Electrothermal actuation is based on the thermal expansion of freestanding beams when subjected to Joule heating. As a result of the voltage applied across the inclined beams (V-shaped beams), the actuator shuttle moves forward [17]. Hence, the design of the thermal actuators requires a two-step analysis: an electrothermal analysis to obtain the temperature distributions and a thermostructural analysis to obtain the displacement fields. For details on the analysis procedure, please refer to [18].

Fig. 2 presents a typical configuration of the ETAs that are used in our investigations. It includes five pairs of V-shaped beams (300  $\mu\text{m}$  long, 8  $\mu\text{m}$  wide, and 3.5  $\mu\text{m}$  thick) and three pairs of heat sink beams (40  $\mu\text{m}$  long, 4  $\mu\text{m}$  wide, and 3.5  $\mu\text{m}$  thick) at each end. The heat sink beams are designed to reduce the temperature at the actuator–specimen interface [18]. For a complete characterization of the electrothermostructural response of an ETA in vacuum, a 3-D finite element analysis using ANSYS multiphysics was pursued. The element type was SOLID 98. The boundary conditions included electric, thermal, and structural domains. The electrical boundary condition was the applied voltage at the two anchors of the V-shaped beams. Thermal and structural boundary conditions were room temperature and zero displacement for all kinematic degrees of freedom at the anchors of the V-shaped and the heat sink beams. Material properties used in these simulations are listed in Table I. Fig. 2(a) and (b) shows the temperature increase and the displacement in the  $y$ -direction, respectively, for an actuation voltage of 1 V in vacuum. It can be seen that the highest temperature increase occurs in the shuttle. Due to thermal expansion, the shuttle displacement is not uniform, as shown in Fig. 2(b).

ETA stiffness with the addition of heat-sink beams is given by

$$K_A = 2N \left( \sin^2 \theta \frac{Ebh}{l} + \cos^2 \theta \frac{Eb^3h}{l^3} \right) + 2n \frac{Eb_{sb}^3h}{l_{sb}^3} \quad (1)$$

where  $N$  is the number of V-shaped beams,  $\theta$  is the angle between the V-shaped beams and the transverse direction,  $E$  is the Young's modulus of the ETA material (polysilicon in our applications),  $h$  is the beam height,  $l$  and  $b$  are the length and width of the V-shaped beams, respectively,  $n$  is the number of pairs of heat sink beams, and  $l_{sb}$  and  $b_{sb}$  are the length and width of the heat sink beams, respectively.

The force that is generated by the ETA is given by

$$F = 2NEA\alpha\Delta T \sin \theta \quad (2)$$

where  $\alpha$  is the polysilicon thermal expansion coefficient,  $\Delta T$  is the average temperature of a V-shaped beam, and  $A$  is the cross-sectional area of a V-shaped beam.

In order to have a stable actuation and pull the specimen in a displacement-controlled fashion, beam angles between  $10^\circ$  and  $30^\circ$  were identified as optimal [18]. Furthermore, the multiphysics analyses showed that the actuator–specimen interface temperature increase can be controlled to a good

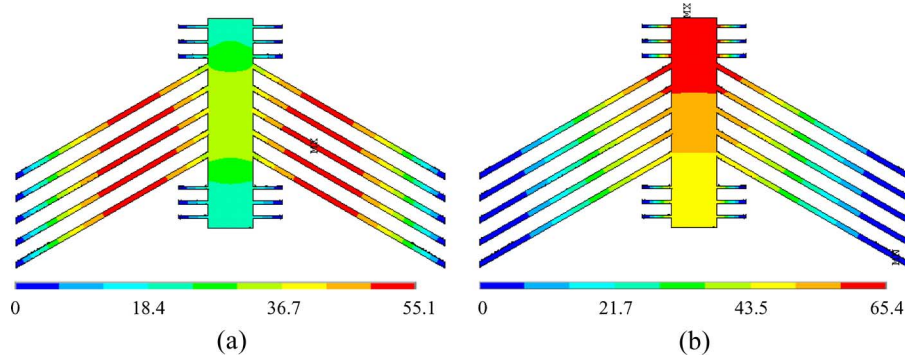


Fig. 2. Contour fields for an ETA subjected to an actuation voltage of 1 V in vacuum. The ETA has a  $30^\circ$  beam angle and three pairs of sink beams at each end. (a) Contours of temperature increase in degree Celsius and (b)  $y$ -direction displacement in nanometers.

TABLE I  
POLYSILICON PROPERTIES USED IN THE MULTIPHYSICS SIMULATIONS

Parameter	Units	Value	Ref.
Young's modulus	GPa	170	[23]
Poisson's ratio	-	0.22	[23]
Thermal conductivity	$\text{W m}^{-1} \text{K}^{-1}$	34	[14]
Resistivity	$\text{ohm} \cdot \text{m}$	$3.4 \times 10^{-5}$	[15]
Thermal expansion coefficient	$\text{K}^{-1}$	$2.6 \times 10^{-6}$	[14]

extent. Depending on the material being tested, this feature of the actuator needs to be carefully examined.

### B. Load Sensor and Related Electronics

The load on the specimen is electronically measured by means of a load sensor. The load sensor that we employ is based on differential capacitive sensing of displacement [19], [20] due to its sensitivity and linear behavior within the displacement range that is needed to investigate nanostructures. Through a proper calibration of the load sensor stiffness, the load can be computed, and a calibration equation is therefore identified [21].

The differential capacitive sensor consists of one set of movable electrodes (fingers) and two sets of stationary electrodes (fingers), as shown in the left portion in Fig. 3(a). Initially, each movable finger is equally spaced between two stationary fingers. The displacement of the movable fingers is equal to the deflection of the folded beams in the axial direction. There is a variety of circuit configurations to realize capacitance measurements [19], [20]. Fig. 3(a) shows the schematic of the charge-sensing method that is used in our approach. This method can effectively mitigate the effect of parasitic capacitances that generally exist in electrostatic MEMS devices. In brief, change of the output voltage  $V_{\text{sense}}$  is proportional to the capacitance change, namely,

$$\Delta V_{\text{sense}} = \frac{V_0}{C_f} \Delta C \quad (3)$$

where  $\Delta V_{\text{sense}}$  is the change of the output voltage,  $V_0$  is the amplitude of an ac voltage signal that is applied to the stationary fingers, and  $C_f$  is the feedback capacitor, as shown in Fig. 3(a).

In order to achieve high-resolution capacitance measurements, it is critical to minimize stray capacitance and electro-

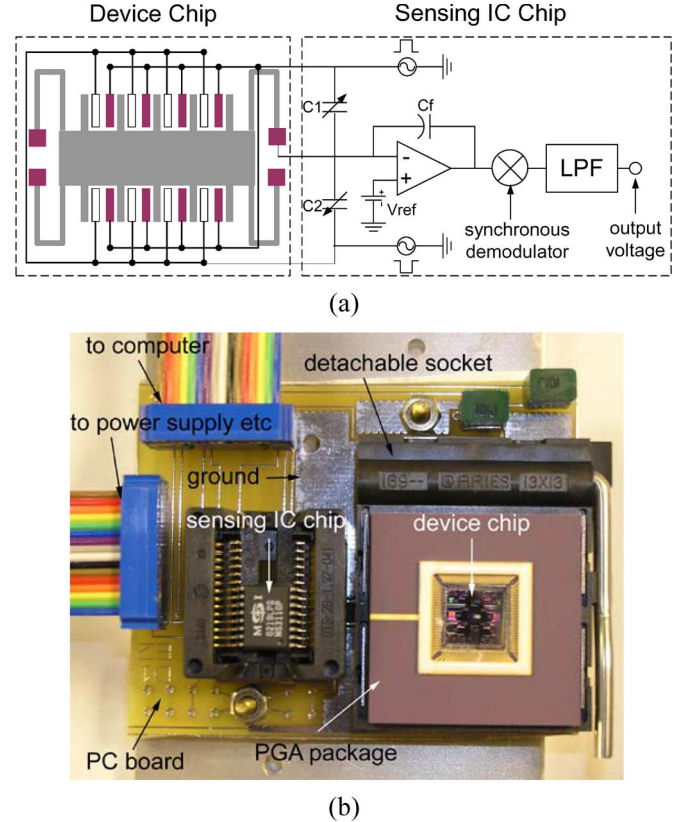


Fig. 3. (a) Double-chip architecture used for measuring capacitance change. Schematic of differential capacitor and signal conditioning circuit. (b) PC board containing both MEMS device chip and sensing IC chip with accessory electronics.

magnetic interference. By integrating the MEMS differential capacitor and the sensing electronics (CMOS) on one chip, the charge-sensing method is able to detect the capacitance change at attofarad level [19]. However, this would significantly

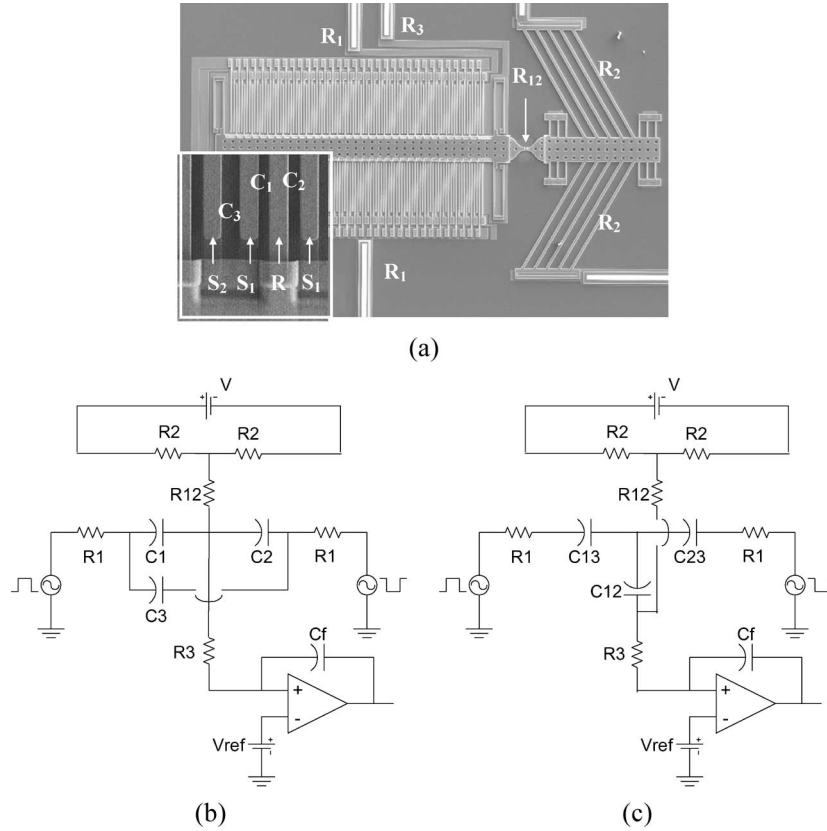


Fig. 4. (a) Device with ETA and corresponding resistances and capacitances. Inset shows the details of movable finger and stationary fingers.  $R_2$  denotes the resistance of the thermal beams,  $R_{12}$  denotes the resistance of the specimen,  $R_1$  and  $R_3$  denote the resistances of the electric traces,  $C_1$  and  $C_2$  denote the capacitances between the movable beams and the two stationary beams, respectively,  $C_3$  denotes the capacitance between two nearby stationary beams. (b) Electric circuit for the device in (a). (c) Equivalent circuit to that in (b) after a  $\Delta - Y$  transformation.

increase the fabrication complexity, rendering it unpractical for our application. An alternative is to use a two-chip architecture, i.e., a MEMS chip containing the devices that are shown in Fig. 1, and a CMOS chip with the signal conditioning electronics. In our setup, an integrated circuit (Universal Capacitive Readout MS3110; Microsensors, Costa Mesa, CA) was used to measure the capacitance change. Both the MEMS and the sensing chips were placed on a custom-made printed circuit board with grounded shields on both sides, as shown in Fig. 3(b) [21].

For a device with thermal actuator, specimen, and load sensor, the equivalent electrical circuits are shown in Fig. 4. The load sensor shuttle is electrically connected to the substrate through the anchors. The capacitances are, respectively, given by

$$C_1 = N\varepsilon \left( \frac{A_1}{d_0 + \Delta d} + \frac{A_2}{g} + 0.65 \frac{A_1}{h} \right) \quad (4a)$$

$$C_2 = N\varepsilon \left( \frac{A_1}{d_0 - \Delta d} + \frac{A_2}{g} + 0.65 \frac{A_1}{h} \right) \quad (4b)$$

$$C_3 = N\varepsilon \left( \frac{A_1}{d_3} + 0.65 \frac{A_1}{h} \right) \quad (4c)$$

where  $N$  is the total unit number of differential capacitors,  $A_1$  is the overlapping area of the stationary finger  $S_1$  (or  $S_2$ ) with the movable finger  $R$ ,  $A_2$  is the overlapping area of  $S_1(S_2)$  with the substrate,  $d_0$  is the initial gap between  $S_1(S_2)$  and  $R$ ,  $\Delta d$

is the displacement of  $R$ ,  $d_3$  is the gap between  $S_1$  and  $S_2$ ,  $g$  is the gap between  $S_1(S_2)$  and the substrate, and  $h$  is the finger thickness. In (4a) and (4b), the first term is the capacitance between  $S_1(S_2)$  and  $R$ , the second term is the capacitance between  $S_1(S_2)$  and the substrate that has the same potential as  $R$ , and the third term is the fringe effect. When  $\Delta d = 0$ ,  $C_1 = C_2 \equiv C_0$ .

Since  $d_3$  is comparable to  $d_0$ , it is inaccurate to neglect  $C_3$  in the analysis. The electric circuit for Fig. 4(a) is shown in Fig. 4(b), while Fig. 4(c) shows its equivalent due to a  $\Delta - Y$  transformation [22]. The equivalent capacitances are given by

$$\begin{aligned} C_{13} &= \frac{C_1 C_2 + C_2 C_3 + C_3 C_1}{C_2} \\ C_{23} &= \frac{C_1 C_2 + C_2 C_3 + C_3 C_1}{C_1} \\ C_{12} &= \frac{C_1 C_2 + C_2 C_3 + C_3 C_1}{C_3}. \end{aligned} \quad (5)$$

By combining (4) and (5), we obtain

$$\begin{aligned} C_{13} - C_{23} &= N\varepsilon_0 A_1 \left( 1 + \frac{C_1 + C_2}{C_1 C_2} \right) \left( \frac{1}{d_0 + \Delta d} - \frac{1}{d_0 - \Delta d} \right) \\ &\approx 2N\varepsilon_0 A_1 \frac{1 + 2C_3/C_0}{d_0^2} \Delta d \propto \Delta d \end{aligned} \quad (6a)$$

$$C_{12} = C_1 + C_2 + \frac{C_1 C_2}{C_3} \approx 2C_0 + \frac{C_0^2}{C_3} = \text{const.} \quad (6b)$$

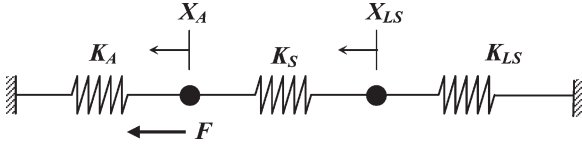


Fig. 5. Schematic of lumped mechanical model for the *in situ* testing device.  $X_S$  is the deformation of the specimen,  $X_{LS}$  is the relative displacement of the load sensor,  $X_A$  is the displacement of the actuator,  $K_S$  is the stiffness of the specimen,  $K_{LS}$  is the stiffness of the load sensor,  $K_A$  is the stiffness of the actuator, and  $F$  is the total force generated by the actuator.

$C_{13} - C_{23}$  is the capacitance difference that we measure in the experiments. The value agreed well with those obtained from finite element simulation [23]. One can notice from (6a) that  $C_{13} - C_{23}$  is larger than  $C_1 - C_2$  for the same displacement  $\Delta d$  by nearly fivefold. This is actually an advantageous feature for the capacitance measurement at subfemtofarad levels.

### C. Lumped Mechanical Model

A lumped model can be used to predict displacements of the actuator, the specimen, and the load sensor as a first-order approximation (Fig. 5). Compatibility of deformation and equilibrium leads to the following system of equations:

$$\begin{aligned} X_{LS} + X_S &= X_A \\ K_{LS}X_{LS} &= K_S X_S \\ K_S X_S + K_A X_A &= F \end{aligned} \quad (7)$$

where  $X_S$  is the deformation of the specimen,  $X_{LS}$  is the displacement of the load sensor,  $X_A$  is the displacement of the actuator,  $K_S$  is the stiffness of the specimen,  $K_{LS}$  is the stiffness of the load sensor,  $K_A$  is the stiffness of the actuator, and  $F$  is the total force that is generated by the actuator, as shown in (2). These equations highlight that the selection of the actuator and load stiffness is a function of the specimen to be tested. Specimens that require a large failure force demand high actuation forces and relatively stiff load sensors. Likewise, depending on the amount of specimen stretching needed to fail, it necessitates particular stiffness ratios between the specimen and the load sensor. To illustrate this point, detailed calculations for the testing of MWCNTs and polysilicon thin films are given in the Appendix.

### D. Fabrication Process

The devices were fabricated by MEMSCAP (Durham, NC). We developed two batches of devices: One is for *in situ* SEM, AFM, and X-ray testing, and the other is for *in situ* TEM testing, which requires the opening of a window underneath the specimen for transmission of the electron beam. The devices for *in situ* SEM, AFM, and X-ray testing were fabricated by following the standard poly-MUMP process. However, for the *in situ* TEM devices, we designed a new process flow on top of the standard poly-MUMPs, which was not commercially available. The challenge in the microfabrication of these devices is due to the requirement of a through-wafer window

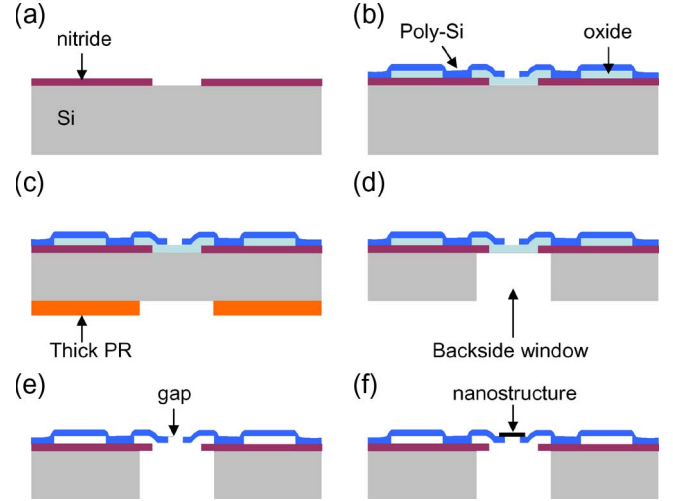


Fig. 6. Fabrication process of the *in situ* TEM testing device. (a) Nitride patterning. (b) Standard poly-MUMPs sample fabrication. (c) Backside grinding and photoresist patterning. (d) DRIE to etch a window. (e) Device release. (f) Mounting nanostructures onto the device.

under the specimen area in order to allow the transmission of the electron beam. The process is detailed in Fig. 6. The process started with the removal of the nitride layer in the specimen area [Fig. 6(a)]. The standard poly-MUMPs were followed to build the device structure [Fig. 6(b)]. After the backside grinding, a thick photoresist layer was spun in the back of the wafer and patterned [Fig. 6(c)]. Deep reactive ion etching (DRIE) was used to etch through the silicon wafer and to stop at the silicon oxide or silicon nitride layers by exploiting etching rate differences [Fig. 6(d)]. After the subdicing, the device was released and super-critical dried [Fig. 6(e)]. All the aforementioned processes were performed at the MUMPs site. After receiving the devices, we positioned the specimens (nanostructures) onto the MEMS devices using a nanomanipulator [Fig. 6(f)] [27]. A device for *in situ* TEM testing is shown in Fig. 1(b), exhibiting the backside window ( $130 \mu\text{m} \times 400 \mu\text{m}$ ). The development of a TEM holder specially to match the *in situ* TEM devices and to facilitate the *in situ* TEM testing is reported elsewhere [15].

## III. DEVICE CHARACTERIZATION AND CALIBRATION

### A. Device Metrology

The metrology characterization of the load sensor was critical in calibrating the capacitance and load measurements, as later described in Section III-C. The out-of-plane profile of the device was measured using an optical profilometer with 2.2-nm vertical resolution (MicroXAM; ADE Phase Shift Technology, Tucson, AZ).

Due to a residual stress gradients, the load sensor is not perfectly planar; rather it shows a bowl-like configuration with a downward curvature (Fig. 7). The profile is along the load sensor shuttle. A maximum vertical offset of about  $1 \mu\text{m}$  between movable and stationary fingers is observed. It was found that the curvature was related to the stiffness of the folded beams. The stiffer the folded beams is, the smaller is the curvature. In this paper, the load sensor with folded beams for testing MWCNTs



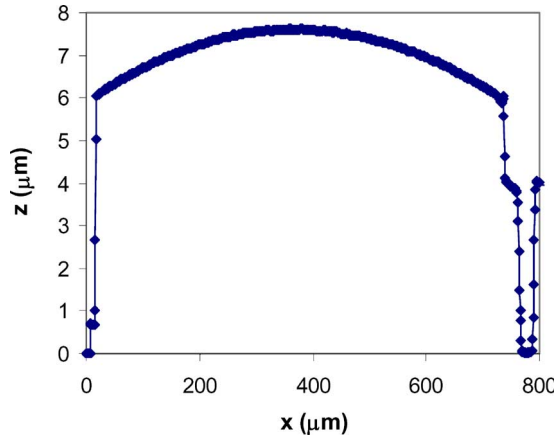


Fig. 7. Out-of-plane profile along the shuttle of the load sensor showing the downward curvature. The horizontal axis is the length along the shuttle, and the vertical axis is the out-of-plane profile. The zero value of the profile corresponds to the substrate.

is discussed. By contrast, the thermal actuator shows excellent planarity.

The beam width was slightly smaller than the designed values probably due to slight over-etching in the MUMPs process. The other observation is that the side walls were trapezoidal. The upper part underwent more over-etching, while the lower part does less. The average gap between movable and stationary fingers  $d_0$  was  $2.8 \mu\text{m}$ , and the average gap between two stationary fingers  $d_1$  was  $3.8 \mu\text{m}$ .

### B. Characterization of the Actuator Performance

It is known that the electric resistivity of polysilicon changes with the temperature. According to our measurements, when the actuation voltage is less than 6 V, the resistance is nearly constant. With a further increase of the actuation voltage, the resistance increases as a result of temperature increase, as shown in the inset in Fig. 8. This is consistent with observations reported in the literature for similar thermal actuators [12], [24]. Fig. 8 also shows the in-plane displacement at the specimen end as a function of the actuation voltage, as measured in an SEM under vacuum. As predicted by the multiphysics finite-element analysis (FEA) simulation that is reported in Section II-B, the highest temperature increase occurs in the shuttle. With no external loading, the shuttle displacement at the specimen end was measured to be 900 nm at an actuation voltage of 8.5 V. From the curve that is plotted in Fig. 8, it is inferred that the displacements are nearly proportional to the input power  $U^2/R$ , where  $U$  is the actuation voltage, and  $R$  is the electrical resistance.

### C. Calibration of the Load Sensor Performance

An important step in the calibration of the load sensor is to obtain the displacement–capacitance change relationship. For this purpose, an otherwise identical device, but without a gap between the actuator and load sensor shuttles, was fabricated on the same chip. The calibration was done inside a field emission SEM (Leo Gemini 1525) by actuating the device at a series of stepwise increasing voltages, which are sequentially applied in

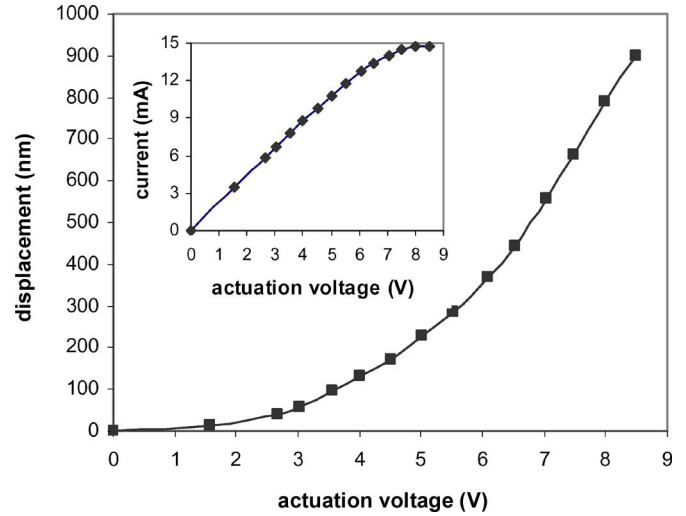


Fig. 8. In-plane displacement at the actuator–specimen interface as a function of the actuation voltage *in situ* the SEM. Inset shows the current–actuation voltage curve for the actuator.

four ON–OFF cycles. The device configuration corresponding to the ON–OFF actuation cycles was captured in one single SEM image, as shown in Fig. 9. Simultaneously, the load sensor output voltage  $V_{\text{sense}}$  was recorded by a digital multimeter and later converted to capacitance change using (3).  $C_f$  was selected such that a 1-mV change in  $V_{\text{sense}}$  corresponded to 1-fF change in capacitance.

The SEM images were analyzed to obtain displacements, following a procedure described in [21]. This image analysis approach has the advantage of eliminating the influence of drift, which is a typical problem in SEM. The data analysis results in subpixel resolution. Fig. 10(a) shows the displacement of the load sensor as a function of the actuation voltage, and Fig. 10(b) shows the corresponding measured capacitance change as a function of the actuation voltage. Fig. 10(c) correlates the displacement and the capacitance change. It follows a linear relationship, which agrees well with (6a). The achievable resolution of the measured capacitance change is approximately 0.05 fF, and the corresponding displacement resolution is 1 nm. We have found that the capacitance measurement has a higher resolution than SEM imaging.

The capacitance change versus displacement can analytically be predicted following the analysis of Section II-B and the device metrology. In the analysis, the downward curvature of the load sensor was taken into account. Fig. 10(c) compares the experimentally obtained and analytically predicted displacement–capacitance change curves. The analytical prediction agrees well with the experimental measurements, within the experimental measuring accuracy.

By following the procedure given in [15], we designed three types of load sensors with different stiffness values (11.8, 48.5, and  $1.22 \times 10^4 \text{ N/m}$ ). The corresponding load resolutions are 11.8 nN, 48.5 nN and  $12.2 \mu\text{N}$ . These three types of load sensors are aimed at testing a spectrum of nanostructures and thin films with different stiffnesses. Note that, by reducing the folded beam stiffness and/or increasing the capacitance measurement resolution using a resonance shift method [12],

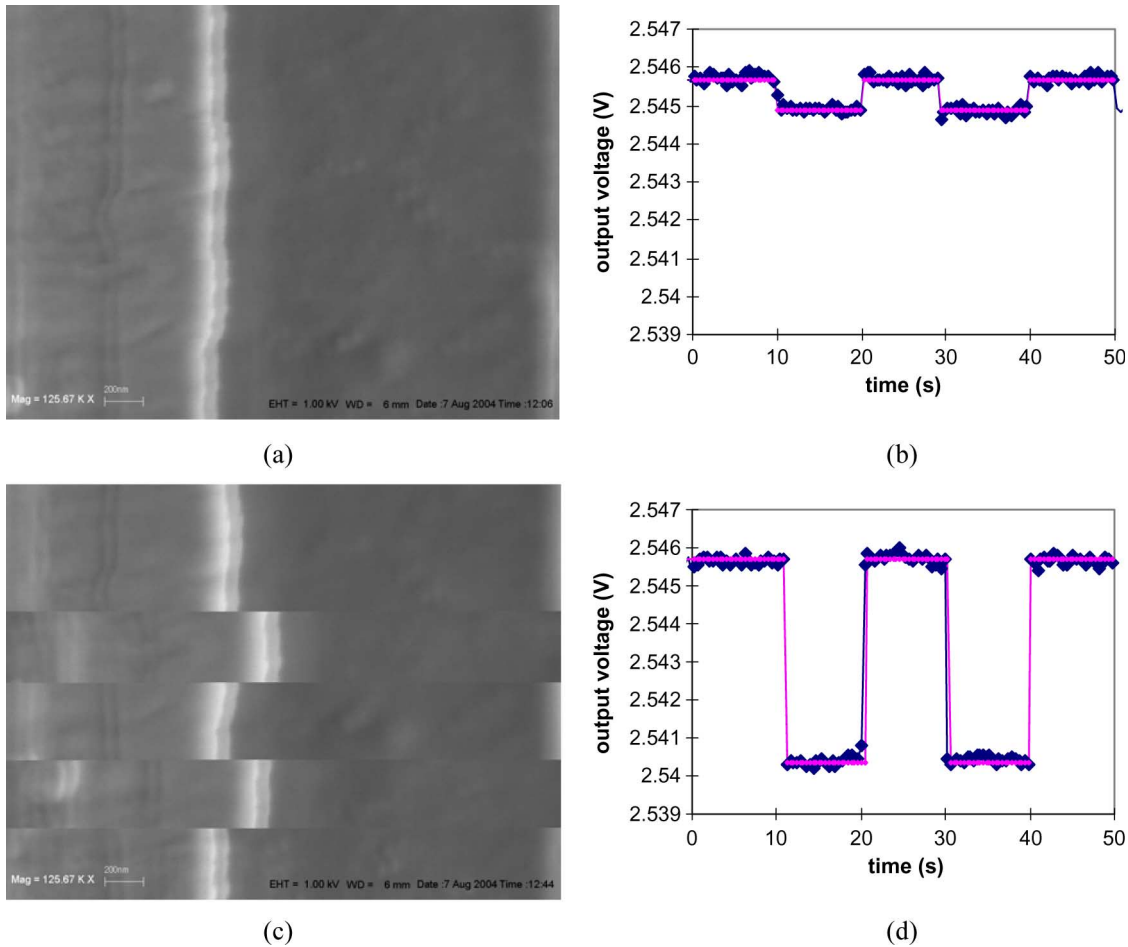


Fig. 9. Displacements of the load sensor captured in SEM images and corresponding capacitance measurements at different actuation voltages. (a), (b) At 2 V. (c), (d) At 5 V. Both raw data and fitted data are shown in the plots.

subnano-Newton load resolutions are achievable with this device.

#### IV. APPLICATIONS

Two types of structures, freestanding polysilicon films and carbon nanotubes, were tested inside an SEM and a TEM to demonstrate the MEMS-based material testing system performance.

The first test results reported here correspond to cofabricated polysilicon specimens. Polysilicon was selected as a test material because of its well-characterized Young's modulus and failure strength [25]–[28]. Since the minimum feature size achievable by a standard photolithography is about  $2\text{ }\mu\text{m}$ , in order to test the nanometer size specimens, the cofabricated freestanding poly-Si specimen was further nano-machined by focused ion beam (FIB). A dog-bone-shaped poly-Si specimen with a trapezoidal cross section was obtained [Fig. 11(a)]. Two platinum (Pt) lines were deposited as reference marks by electron beam induced deposition (EBID) [15] in a FIB/SEM dual beam instrument (FEI, Hillsboro, OR). Sample elongation during loading was measured by means of a custom-developed software [21]. The stress–strain curve of a typical polysilicon specimen is shown in Fig. 11(b). The scatter in the data illustrates measurement accuracy. Load accuracy

was  $\pm 12.2\text{ }\mu\text{N}$ , and the corresponding stress accuracy was  $\pm 17.5\text{ MPa}$ . Displacement accuracy from the SEM measurement was estimated to be  $\pm 2\text{ nm}$ , and the strain accuracy was  $\pm 0.09\%$ . The measured Young's modulus was  $154.5 \pm 12.5\text{ GPa}$ , and the fracture strength was  $1.42 \pm 0.02\text{ GPa}$ . These values are in good agreement with those reported for MUMPs poly-Si thin films. In addition, SEM examination of the failed cross section revealed a mirror region at the top right corner of the fracture surface, which is typical of brittle fracture initiation [10], [27], [28].

The effect of stress concentration was also investigated in cofabricated polysilicon specimens containing circular holes. Two tests were performed on specimens that are  $3.8\text{ }\mu\text{m}$  wide with holes that are  $2.2$  and  $2.8\text{ }\mu\text{m}$  in diameter. Fig. 12(a) shows the sample geometry and a FIB-machined hole in the gauge region. Fig. 12(b) reports the measured force–displacement curve for both sample 1 (hole diameter =  $2.2\text{ }\mu\text{m}$ ) and sample 2 (hole diameter =  $2.8\text{ }\mu\text{m}$ ). The specimen response is initially linear elastic until a sudden drop in force. It is interesting to note that a load increase is subsequently needed to produce the complete failure of the samples, with the specimen containing the smallest hole diameter exhibiting a stiffer behavior. It should be noted that the identified response was only possible because of the displacement control characteristics of the thermal actuator, which, in turn, resulted in a stable deformation path.

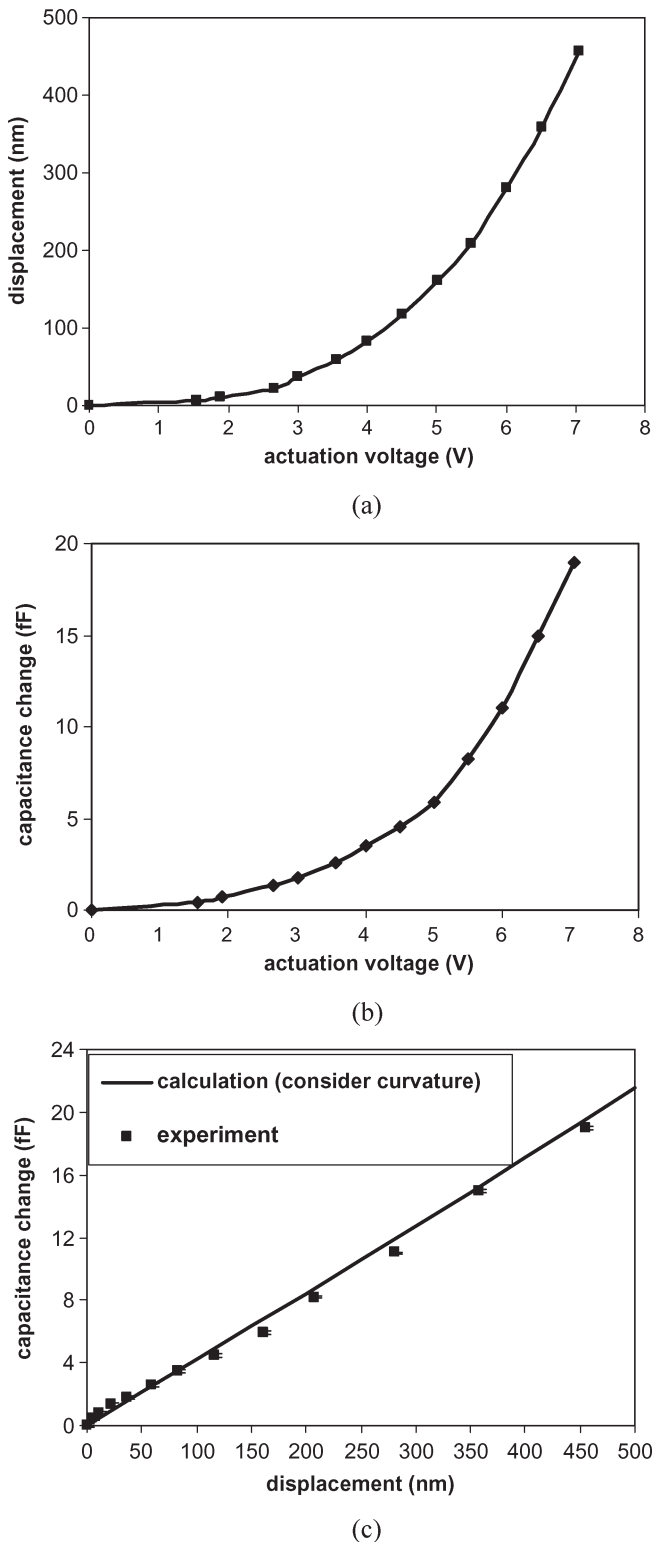
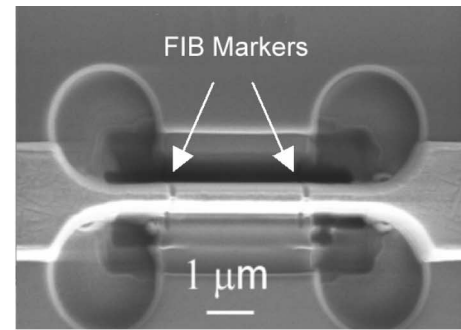
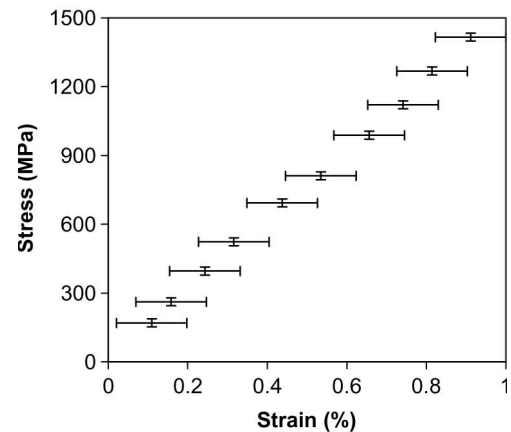


Fig. 10. (a) Displacements obtained from image analysis at different actuation voltages. (b) Capacitance change at different actuation voltages. (c) Calibration of displacement as a function as the measured capacitance change and comparison with the calculation considering the load sensor curvature and measured metrology.

This feature is of particular relevance in the investigation of nanoscale damage and inelasticity kinetics, as it is briefly demonstrated here. Damage initiation is likely the result of microcracks that are initiated on the edges of the hole (region of



(a)



(b)

Fig. 11. (a) FIB-machined dog-bone-shaped polysilicon specimen with two platinum markers at the gauge region. (b) Stress-strain curve of the polysilicon films. The specimen is 6  $\mu\text{m}$  long and 1.6  $\mu\text{m}$  thick, with a top width of 0.42  $\mu\text{m}$  and bottom width of 1.04  $\mu\text{m}$ .

maximum stress and surface defects). It is known that surface roughness and pitting are the origins of MUMPs polysilicon fracture [29], [30]. In the FIB fabricated holes, the Gallium (Ga) ion beam introduced surface roughness, which could act as crack precursors. As a result, during tensile stretching, microcracks are likely nucleated at the surface defects in the hole surface, which, in turn, resulted in the load reduction that is experimentally observed. From the load-displacement signature, it is clear that the cracking process was stable. A load increase was required for further crack propagation and ultimate failure of the specimen. While the developed nanoscale material testing system could be used to characterize in detail failure initiation and propagation, such effort is beyond the scope of the present paper. Here, we simply illustrate its capabilities.

We have also tested MWCNTs *in situ* the SEM and TEM. The MWCNTs were synthesized on a silicon wafer using the chemical vapor deposition (CVD) method by First Nano, Inc. (Ronkonkoma, NY). The MWCNTs were directly manipulated and mounted on the MEMS device without the purification or ultrasonication steps, which typically introduce large defects [35]. The *in situ* TEM observation revealed that MWCNTs, when exposed to high-energy electron or ion beam irradiation, did not exclusively follow the previously reported "sword-in-sheath" type failure [4], rather they failed in multiple shells or the entire cross sections. Six MWCNTs were tested *in situ* the TEM or SEM [31]. The nanotube geometries, irra-



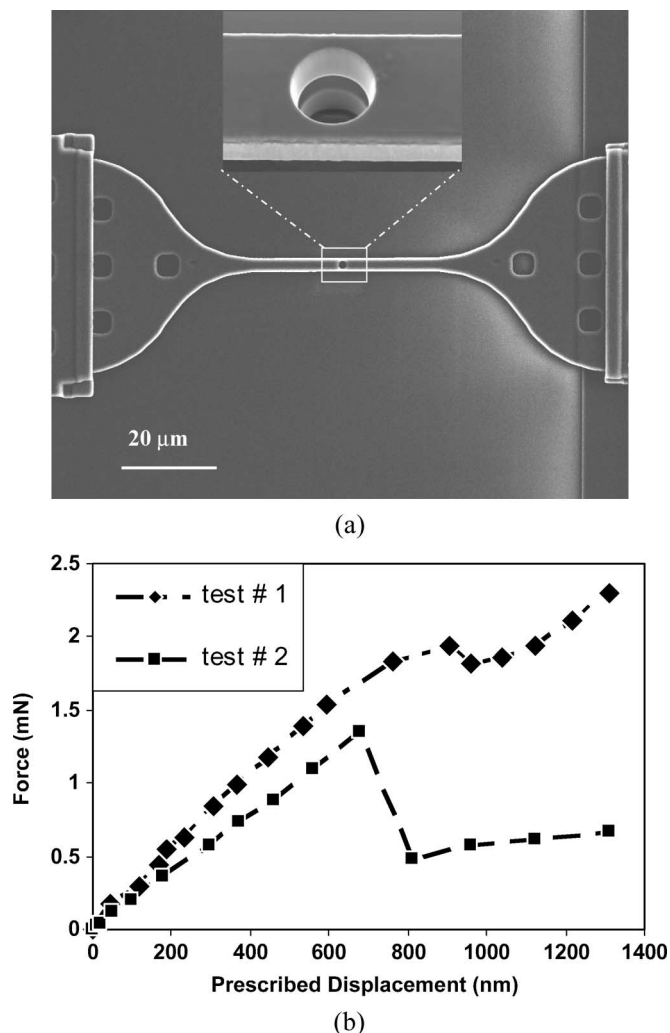


Fig. 12. (a) SEM image of cofabricated polysilicon specimen containing circular holes nanomachined by FIB. (b) Load–displacement curves for two tested samples. Sample 1 containing a circular hole of diameter = 2.2  $\mu\text{m}$  and sample 2 containing a circular hole of diameter = 2.8  $\mu\text{m}$ .

diation conditions, and measurement results are summarized in Table II. Fig. 13(a) is a plot of load–elongation for the tested MWCNTs. The plot shows that, as the irradiation dose increases, the stiffness of the specimen also increases. The reason for this stiffness increase under tensile loading was inferred from the acquired electron microscopy images and the measured load–displacement signatures. These images revealed that, when MWCNTs are subjected to Ga ion beam irradiation (prior to the *in situ* TEM testing), the entire cross section breaks, as shown in Fig. 13(b). By contrast, when MWCNTs are subjected to e-beam irradiation during the *in situ* TEM testing, a telescopic failure is observed, with the number of outer shell undergoing fracture as a function of the irradiation dose. Multiple shells fracturing, rather than only the outer shell, was observed [see Fig. 13(c)]. For experiments that conducted *in situ* the SEM at an operating voltage of 5 kV, a single outer shell failure that is consistent with the previous results reported in the literature [4] was observed. Specimens #1 and 2 in the failure region were only exposed to a Ga ion beam with 30-kV acceleration voltages (not exposed to electron beams). This was the case because the specimens failed in a region

protected by the Si wafer, i.e., outside the electron beam observation window. To image the fracture region within the TEM, after the failure, the thermal actuator was energized to displace the broken end of the specimen to the window region. Specimens #3 and 4 were exposed to electron beams with a 200-kV acceleration voltage (in the TEM). Specimen #5 was exposed to an electron beam with a 5-kV acceleration voltage (in the SEM). Specimen #6 was exposed to both 30-kV Ga ion and 200-kV electron beams. Note that the threshold voltage for an electron beam in removing a carbon atom by a knock-on collision is about 86 kV [32].

Typically, during the tensile testing of MWCNTs, the two ends of the outermost shell are clamped to the testing device using an EBID of platinum [15]. As a result, only van der Waals interactions between shells are expected. Hence, during *in situ* SEM tensile testing (irradiation energy below the threshold for atomic structure modification), only the outermost shell carries the load and breaks. By contrast, our testing reveals that, for those MWCNTs exposed to high-energy electron or ion beam irradiation, multiple shells or the entire cross section breaks. This suggests that the e-beam or ion beam irradiation introduces crosslinks between the shells. This is corroborated in the literature through experimentation and first principle calculations. In fact, it has been reported that, above a certain energy threshold, electron and ion beams can produce vacancies in the nanotube shells and corresponding interstitials in the intershell spacing [32]. Moreover, molecular dynamics simulations revealed that these interstitial atoms can form stable and covalent bonds between shells [33]. The simulations further demonstrated that moderate beam irradiation can increase the failure strength of MWCNTs because of the development of covalent bonds, while excessive irradiation can degrade the MWCNT mechanical properties due to structural damage (cluster of vacancies) and/or amorphization [33], [34]. Our experimental observations are in a good agreement with these simulation predictions.

Another aspect of interest is the stress–strain behavior of the tested MWCNTs, so we present and discuss them in the sequel. Note that, in the process of transforming load–displacement curves into stress–strain curves, the issue on how to define the tube cross-sectional area arises. In previous *in situ* SEM work, when only the outermost shell carries the load, the cross section was defined as  $\text{OD} \times t$  (where OD is the outer diameter of the MWCNT and  $t$  is the intershell spacing, which is about 0.34 nm). However, when crosslinking between multiple shells exists, a new definition for the cross-sectional area is needed. One possibility is to use the imaged number of broken shells in the failed cross section. However, this may overestimate the cross-sectional area since the failure may happen in a number of steps. In other words, the failed cross-sectional area at peak load might be smaller than that observed at a later time. Due to a slow acquisition rate if charge-coupled device (CDD) cameras are used in TEM instruments, such differentiation is currently not possible even in real-time observations. Another possibility is to take the *in situ* SEM measured modulus as the true modulus of the material and to infer the number of failed shells at peak load by matching the calculated Young's modulus. For the MWCNTs tested in this paper, the *in situ* SEM test revealed a Young's

TABLE II  
IRRADIATION CONDITIONS AND MEASURED MECHANICAL PROPERTIES OF MWCNTs. TABULATED ARE THE EXPERIMENT NUMBER, GAUGE LENGTH, OUTER DIAMETER, BEAM TYPE AND DOSE, FAILURE FORCE, FAILURE ELONGATION, AND THE NUMBER OF SHELLS USED IN STRESS CALCULATIONS

Experiment Number	L ( $\mu\text{m}$ )	OD (nm)	Ion irradiation dose ( $\text{e cm}^{-2}$ )	Electron irradiation dose ( $\text{e cm}^{-2}$ )	F ( $\mu\text{N}$ )	$\Delta d$ (nm)	Effective # of broken shells
1	6.69	191	$10^{14}$	-	31.1	195.6	13
2	3.02	142	$0.5 \times 10^{14}$	-	20.4	101.2	11
3	2.85	169	-	$4.5 \times 10^{21}$	9.9	143.8	5
4	3.3	108	-	$1.5 \times 10^{21}$	4.3	97.5	3
5	3.82	96	-	-	1.9	221.9	1
6	2.57	130	$10^{14}$	$15 \times 10^{21}$	2.2	40	-

Note: the effective number of shells is determined by matching the Young's modulus to that in which only one shell fractured (Test #5: in-situ SEM experiment and lowest irradiation dose). For the same dose, the Ga ion beam has orders of magnitude stronger effect on the MWCNTs than electron beam due to its heavier atomic mass [34].

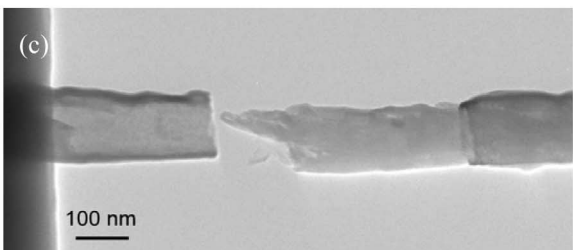
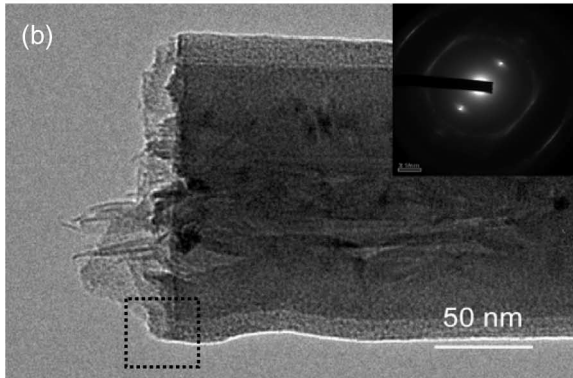
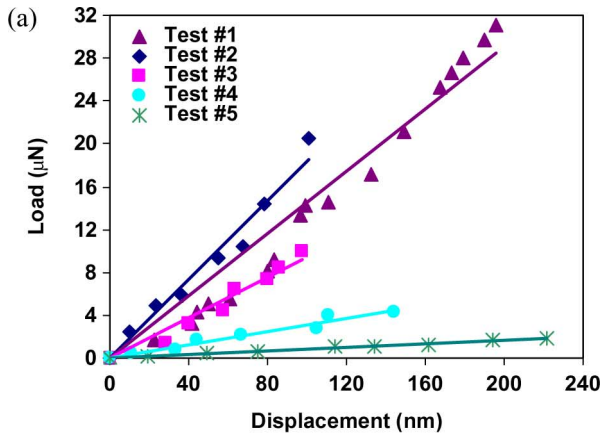


Fig. 13. (a) Load-elongation measurements corresponding to CVD-grown MWCNT specimens tested under various irradiation conditions. Note that specimen #1 does not possess the highest stiffness despite being exposed to the highest Ga ion irradiation because its length is about twice that of specimen #2. Its stiffness is the highest if normalized by the length. Refer to Table II for the maximum load and displacement. Test #6 is not plotted because it failed prematurely, likely due to heavy ion and electron irradiation. (b) Typical fracture surface of an MWCNT subjected to ion beam irradiation showing failure of the entire cross-sectional area (Test #1). (c) Typical fracture surface of an MWCNT subjected to e-beam irradiation at 200 kV, showing telescopic failure with multiple-shells broken (Test #4).

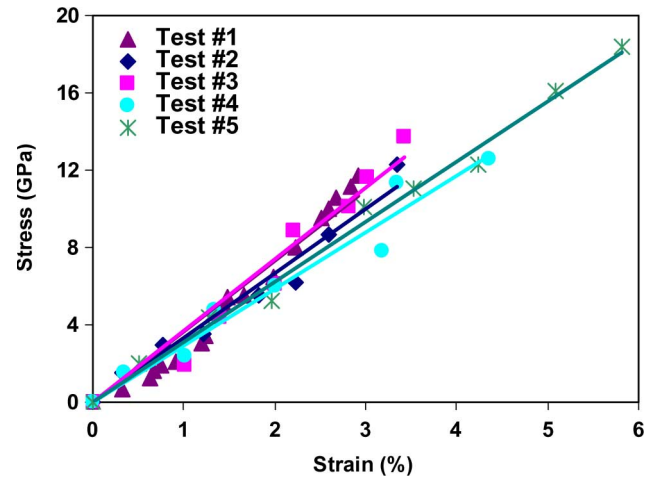


Fig. 14. Stress-strain curves for the tested MWCNTs. See text for definition of cross-sectional area.

modulus of  $315 \pm 11$  GPa, which is close to that reported for arc-grown MWCNT [4]. Fig. 14 plots the stress-strain curves that are obtained for the tested MWCNTs when subjected to various irradiation conditions. The number of shells that is used in the calculations is reported in the same figure. Failure stresses in the range of 12–20 GPa were measured. Note that these stresses are well below the theoretical stresses that are predicted for single-walled carbon nanotubes using quantum and molecular mechanics simulations [35]. These authors demonstrate that defects of a few nanometers in size are needed to explain the measured failure stresses. A distribution of such defects along the tube length would also explain the low modulus that is experimentally measured.

## V. CONCLUSION

A novel MEMS-based material testing system for *in situ* electron and probe microscopy (AFM, SEM, and TEM) testing of nanostructures has been developed. The testing system provides a continuous observation of specimen deformation and failure at subnanometer resolution, while simultaneously measuring the applied load electronically with nano-Newton resolution. In this regard, it overcomes limitations of other existing approaches. We have discussed the design, fabrication, and calibration of the testing system. Particular emphasis

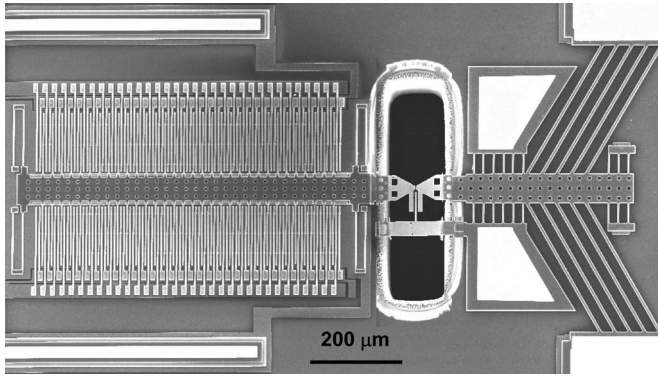


Fig. 15. MEMS-based material testing system for *in situ* TEM compressive and indentation testing of nanostructures.

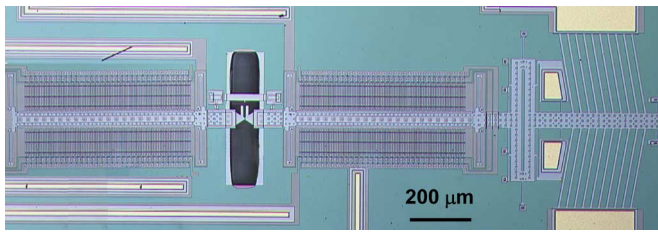


Fig. 16. MEMS-based material testing system for *in situ* TEM testing of nanostructures with both electronic reading of load and relative sample deformation. Two differential capacitors on each side of the specimen are incorporated in the system.

was placed in the appropriate selection of actuator and load sensor stiffness as a function of the sample geometry and expected material behavior. Moreover, the utility of the device has been demonstrated by testing freestanding polysilicon films and MWCNTs *in situ* the SEM and TEM, respectively. The device achieved resolutions of 0.05 fF in capacitance, 1 nm in displacement, and 12 nN in load.

We have also presented the fabrication steps that are needed to open a window underneath the specimen to make possible the transmission of electrons, which is needed in *in situ* TEM studies. Likewise, the reader should note that simple modifications of the device make possible loading conditions beyond simple tension. For instance, in Fig. 15, a device that is designed for compression testing of nanostructures is shown. In this case, the orientation of the inclined beams in the thermal actuator is reversed, such that its motion is toward the load sensor. A natural extension of the setup allows the performance of *in situ* indentation tests. In this configuration, a nanowire or MWCNT with the function of indenter can be mounted by nanomanipulation on the actuator shuttle.

Another important feature of the developed device is the capability of electronically measuring not only the load but also the average specimen deformation. In this case, two differential capacitors, one on each side of the specimen, are required. Fig. 16 shows a testing system microfabricated to achieve this feature. In addition, note that all the ideas and analyses presented in this paper, including the lumped model analysis, can be extended to such configuration and others.

In closing, we expect that the developed MEMS-based material testing system will have a similar impact and produce the

same level of opportunities as the development of the universal testing machine in the last century.

## APPENDIX

The testing of a MWCNT in a device containing a thermal actuator with five pairs of V-shaped beams and six pairs of heat sink beams is analyzed here. The stiffness of the load sensor is computed to achieve a 1-μN failure load and a specimen failure strain of 4%. Following (1), the stiffness of the thermal actuator is

$$K_A = 10 \left( \sin^2 \theta \frac{Ebh}{l} + \cos^2 \theta \frac{Eb^3h}{l^3} \right) + \frac{12Eb_{sb}^3h}{l_{sb}^3} = 46892 \text{ N/m}$$

where  $E = 170 \text{ GPa}$  [24],  $l = 300 \text{ μm}$ ,  $b = 8 \text{ μm}$  (V-shaped beam width),  $h = 3.5 \text{ μm}$  (V-shaped beam height),  $\theta = 30^\circ$ ,  $b_{sb} = 4 \text{ μm}$ , and  $l_{sb} = 40 \text{ μm}$ .

The load sensor is supported by four pairs of folded beams. Its stiffness is given by

$$K_L = \frac{24EI}{l_L^3} = \frac{2Eb_L^3h_L}{l_L^3} = 18.6 \text{ N/m}$$

where  $l_L = 200 \text{ μm}$  (folded beam length),  $b_L = 5 \text{ μm}$  (folded beam width), and  $h_L = 3.5 \text{ μm}$  (folded beam height).

The stiffness of the CNT is

$$K_S = \frac{E_s A}{l_s} = \frac{E_s \pi D_o t}{l_s} = 10.7 \text{ N/m}$$

where  $D_o = 20 \text{ nm}$  is the outermost diameter for the tube,  $t = 0.34 \text{ nm}$  is the interlayer spacing of graphite,  $E_s \approx 1 \text{ TPa}$  is the Young's modulus of CNTs [4], and  $l_s = 2 \text{ μm}$  is the specimen length.

Note that the stiffness of the load sensor and the specimen are much smaller than that of the thermal actuator, which confirms that the testing system works in a displacement-controlled mode. By assuming that the failure force of the CNT is 1000 nN, the solution of (7) results in the following displacements:

$$X_L = 53.8 \text{ nm}$$

$$X_S = 93.5 \text{ nm}$$

$$X_A = 157.3 \text{ nm}.$$

This actuator displacement is easily achievable within the range of actuation voltages that are experimentally identified. Moreover, according to multiphysics analysis, the temperature increase at the thermal actuator–specimen interface is about 75 °C for the case with three pairs of sink beams and about 30 °C for six pairs of sink beams. Both of these temperature increases are quite moderate and should not affect the stress–strain response of the tested nanostructure.

The testing of a polysilicon freestanding film with a device containing a thermal actuator consisting of ten pairs of

V-shaped beams and six pairs of heat sink beams is next analyzed. Following (1), the stiffness of the thermal actuator is

$$K_A = 20 \left( \sin^2 \theta \frac{Ebh}{l} + \cos^2 \theta \frac{Eb^3h}{l^3} \right) + \frac{12Eb_{sb}^3h}{l_{sb}^3} \\ = 86\,644 \text{ N/m.}$$

The load sensor is supported by two pairs of arclike folded beams that are close to the specimen end and two pairs of much more compliant folded beams at the other end. The arclike structure was chosen to achieve enough stiffness in the load sensor and to reduce stress concentrations in the beams. The straight part of the beam is  $125 \mu\text{m}$  long and  $35 \mu\text{m}$  wide, and the arc part has an inner radius of  $35 \mu\text{m}$  and outer radius of  $70 \mu\text{m}$ . Due to the complex shape, a finite-element analysis was used to calculate the sensor stiffness, which resulted in a value of  $3020 \text{ N/m}$ .

By considering a polysilicon specimen with trapezoidal cross section, with a width spanning from  $0.42 \mu\text{m}$  (top) to  $1.04 \mu\text{m}$  (bottom), a thickness of  $1.6 \mu\text{m}$ , and a gauge length  $l_s = 4.7 \mu\text{m}$ , its stiffness is

$$K_S = \frac{E_s A}{l_s} = 42 \times 10^3 \text{ N/m}$$

where  $E_s$  is the Young's modulus of polysilicon.

For the optimal performance of the device, specimen stiffness needs be comparable to that of the load sensor. Moreover, the arclike folded beam stiffness should be comparable to the specimen stiffness. By assuming a failure strain of the polysilicon sample to be 1%, the solution of (7) results in the following displacements:

$$X_L = 655 \text{ nm} \\ X_S = 47 \text{ nm} \\ X_A = 702 \text{ nm.}$$

This actuator displacement is achievable within the range of actuation voltages that are experimentally identified. According to multiphysics analysis, the temperature increase of the thermal actuator close to the specimen is about  $320^\circ\text{C}$  for the case of three pairs of sink beams and about  $130^\circ\text{C}$  for six pairs of sink beams.

#### ACKNOWLEDGMENT

The authors would like to thank C.-M. Li for the TEM imaging of carbon nanotubes. The TEM holder that was used in this investigation was provided by Prof. I. Petrov from the Frederick Seitz Materials Research Laboratory. SEM calibration and testing were performed at the EPIC facility of the NUANCE Center at Northwestern University.

#### REFERENCES

- [1] A. M. Fennimore, T. D. Yuzvinsky, W. Q. Han, M. S. Fuhrer, J. Cummings, and A. Zettl, "Rotational actuator based on carbon nanotubes," *Nature*, vol. 424, no. 6947, pp. 408–410, Jul. 2003.
- [2] M. M. J. Treacy, T. W. Ebbesen, and J. M. Gibson, "Exceptionally high Young's modulus observed for individual carbon nanotubes," *Nature*, vol. 381, no. 6584, pp. 678–680, Jun. 1996.
- [3] E. W. Wong, P. E. Sheehan, and C. M. Lieber, "Nanobeam mechanics: Elasticity, strength, and toughness of nanorods and nanotubes," *Science*, vol. 277, no. 5334, pp. 1971–1975, Sep. 1997.
- [4] M. F. Yu, O. Lourie, M. J. Dyer, K. Moloni, T. F. Kelly, and R. S. Ruoff, "Strength and breaking mechanism of multiwalled carbon nanotubes under tensile load," *Science*, vol. 287, no. 5453, pp. 637–640, Jan. 2000.
- [5] P. A. Williams, S. J. Papadakis, M. R. Falvo, A. M. Patel, M. Sinclair, A. Seeger, A. Helser, R. M. Taylor, II, S. Washburn, and R. Superfine, "Controlled placement of an individual carbon nanotube onto a microelectromechanical structure," *Appl. Phys. Lett.*, vol. 80, no. 14, pp. 2574–2576, Apr. 2002.
- [6] L. L. Chu, L. Que, and Y. B. Gianchandani, "Measurements of material properties using differential capacitive strain sensors," *J. Microelectromech. Syst.*, vol. 11, no. 5, pp. 489–498, Oct. 2002.
- [7] Y. Lai, J. McDonald, M. Kujath, and T. Hubbard, "Force, deflection and power measurements of toggled microthermal actuators," *J. Micromech. Microeng.*, vol. 14, no. 1, pp. 49–56, Jan. 2004.
- [8] R. Hickey, M. Kujath, and T. Hubbard, "Heat transfer analysis and optimization of two-beam microelectromechanical thermal actuators," *J. Vac. Sci. Technol. A, Vac. Surf. Films*, vol. 20, no. 3, pp. 971–974, May 2002.
- [9] J. K. Luo, A. J. Flewitt, S. M. Spearing, N. A. Fleck, and W. I. Milne, "Three types of planar structure microspring electro-thermal actuators with insulating beam constraints," *J. Micromech. Microeng.*, vol. 15, no. 8, pp. 1527–1535, Aug. 2005.
- [10] H. Kahn, R. Ballarini, R. L. Mullen, and A. H. Heuer, "Electrostatically actuated failure of microfabricated polysilicon fracture mechanics specimens," *Proc. R. Soc. Lond. A, Math. Phys. Sci.*, vol. 455, no. 1990, pp. 3807–3823, Oct. 1999.
- [11] M. T. A. Saif and N. C. MacDonald, "A millinewton microloading device," *Sens. Actuators A, Phys.*, vol. 52, no. 1, pp. 65–75, Mar. 1996.
- [12] L. L. Chu and Y. B. Gianchandani, "A micromachined 2D positioner with electrothermal actuation and subnanometer capacitive sensing," *J. Micromech. Microeng.*, vol. 13, pp. 279–285, 2003.
- [13] L. Yin and G. K. Ananthasuresh, "A novel topography design scheme for the multi-physics problems of electro-thermally actuated compliant micromechanism," *Sens. Actuators A, Phys.*, vol. 97/98, pp. 599–609, 2002.
- [14] M. A. Haque and M. T. A. Saif, "Application of MEMS force sensors for in-situ mechanical characterization of nanoscale thin films in SEM and TEM," *Sens. Actuators A, Phys.*, vol. 97/98, pp. 239–245, 2002.
- [15] Y. Zhu and H. D. Espinosa, "An electromechanical material testing system for *in situ* electron microscopy and applications," *Proc. Nat. Acad. Sci.*, vol. 102, no. 41, pp. 14 503–14 508, Oct. 2005.
- [16] M. Zhang, E. A. Olson, R. D. Twisten, J. G. Wen, L. H. Allen, I. M. Robertson, and I. Petrov, "In situ transmission electron microscopy studies enabled by microelectromechanical system technology," *J. Mater. Res.*, vol. 20, pp. 1802–1807, 2005.
- [17] L. Que, J.-S. Park, and Y. B. Gianchandani, "Bent-beam electrothermal actuators—Part I: Single beam and cascaded devices," *J. Microelectromech. Syst.*, vol. 10, no. 2, pp. 247–254, Jun. 2001.
- [18] Y. Zhu, A. Corigliano, and H. D. Espinosa, "A thermal actuator for nanoscale *in situ* microscopy testing: Design and characterization," *J. Micromech. Microeng.*, vol. 16, no. 2, pp. 242–253, Feb. 2006.
- [19] B. E. Boser, "Electronics for micromachined inertial sensors," in *Proc. Transducers*, Chicago, IL, Jun. 16–19, 1997, pp. 1169–1172.
- [20] S. D. Senturia, *Microsystem Design*. Boston, MA: Kluwer, 2002.
- [21] Y. Zhu, N. Moldovan, and H. D. Espinosa, "A microelectromechanical load sensor for *in situ* electron and X-ray microscopy tensile testing of nanostructures," *Appl. Phys. Lett.*, vol. 86, no. 1, p. 013 506, Jan. 2005.
- [22] V. Del Toro, *Engineering Circuits*. Englewood Cliffs, NJ: Prentice-Hall, 1986.
- [23] A. Corigliano, B. De Masi, A. Frangi, C. Comi, A. Villa, and M. Marchi, "Mechanical characterization of polysilicon through on-chip tensile tests," *J. Microelectromech. Syst.*, vol. 13, no. 2, pp. 200–219, Apr. 2004.
- [24] A. A. Geisberger, N. Sarkar, M. Ellis, and G. D. Skidmore, "Electrothermal properties and modeling of polysilicon microthermal actuators," *J. Microelectromech. Syst.*, vol. 12, no. 4, pp. 513–523, Aug. 2003.
- [25] W. N. Sharpe, Jr., K. M. Jackson, K. J. Hemker, and Z. Xie, "Effect of specimen size on Young's modulus and fracture strength of polysilicon," *J. Microelectromech. Syst.*, vol. 10, no. 3, pp. 317–326, Sep. 2001.
- [26] I. Chasiotis and W. G. Knauss, "A new microtensile tester for the study of MEMS materials with the aid of atomic force microscopy," *Exp. Mech.*, vol. 42, no. 1, pp. 51–57, Mar. 2002.
- [27] T. Tsuchiya, O. Tabata, J. Sakata, and Y. Taga, "Specimen size effect on tensile strength of surface-micromachined polycrystalline silicon thin films," *J. Microelectromech. Syst.*, vol. 7, no. 1, pp. 106–113, Mar. 1998.
- [28] S. Greek, F. Ericson, S. Johansson, and J.-Å. Schweitz, "In situ tensile strength measurement and Weibull analysis of thick film and thin film

micromachined polysilicon structures,” *Thin Solid Films*, vol. 292, no. 1/2, pp. 247–254, Jan. 1997.

- [29] I. Chasiotis and W. G. Knauss, “The mechanical strength of polysilicon films: Part 2. Size effects associated with elliptical and circular perforations,” *J. Mech. Phys. Solids*, vol. 51, no. 8, pp. 1551–1572, Aug. 2003.
- [30] I. Chasiotis and W. G. Knauss, “The mechanical strength of polysilicon films: Part 1. The influence of fabrication governed surface conditions,” *J. Mech. Phys. Solids*, vol. 51, no. 8, pp. 1533–1550, Aug. 2003.
- [31] Y. Zhu and H. D. Espinosa, 2006, manuscript in preparation.
- [32] B. W. Smith and D. E. Luzzi, “Electron irradiation effects in single wall carbon nanotubes,” *J. Appl. Phys.*, vol. 90, no. 7, pp. 3509–3515, Oct. 2001.
- [33] M. Huhtala, A. V. Krashennnikov, J. Aittoniemi *et al.*, “Improved mechanical load transfer between shells of multiwalled carbon nanotubes,” *Phys. Rev. B, Condens. Matter*, vol. 70, no. 4, p. 045 404, Jul. 2004.
- [34] J. A. V. Pomoell, A. V. Krashennnikov, K. Nordlund *et al.*, “Ion ranges and irradiation-induced defects in multiwalled carbon nanotubes,” *J. Appl. Phys.*, vol. 96, no. 5, pp. 2864–2871, Sep. 2004.
- [35] S. L. Zhang, S. L. Mielke, R. Khare *et al.*, “Mechanics of defects in carbon nanotubes: Atomistic and multiscale simulations,” *Phys. Rev. B, Condens. Matter*, vol. 71, no. 11, p. 115 403, Mar. 2005.
- [36] *MUMPs Web*. [Online]. Available: <http://www.memsrus.com/>

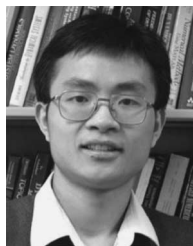


**Horacio D. Espinosa** received the undergraduate degree in civil engineering from Northeast National University, Argentina, the M.Sc. degree in structural engineering from the Politecnico di Milano, Milan, Italy, and the Ph.D. degree in applied mechanics from Brown University, Providence, RI, in 1992.

He was a member of the faculty at Purdue University, West Lafayette, IN, and later moved to Northwestern University, Evanston, IL, in 2000, where he is currently a Professor of mechanical engineering.

He has made contributions in the areas of dynamic failure of advanced materials and micro- and nanomechanics. He has published over 150 technical papers in these fields. His research interests include size scale plasticity and fracture of nanostructures, microelectromechanical and nanoelectromechanical systems, *in situ* electron and atomic probe microscopy testing of nanostructures, and the development of devices for massively parallel atomic probe microscopy writing with chemicals and bio-molecules.

Prof. Espinosa has received numerous awards and honors recognizing his research and teaching efforts, including two Young Investigator Awards, NSF-Career and ONR-YIP, the American Academy of Mechanics (AAM) 2002—Junior Award, the Society of Experimental Mechanics 2005 Hetenyi Award (Best Paper of the Year Award), and, recently, the Society of Engineering Science (SES) 2007 Junior Medal. He is a Fellow of the AAM and of the American Society of Mechanical Engineers (ASME). He was the Editor of *Mechanics*, a publication of the AAM, and currently serves as the Editor-in-Chief of the *Journal of Experimental Mechanics* and as an Associate Editor of the *Journal of Applied Mechanics*.



**Yong Zhu** received the B.S. degree from the University of Science and Technology of China, Hefei, China, in 1999, and the M.S. and Ph.D. degrees in mechanical engineering from Northwestern University, Evanston, IL, in 2001 and 2005, respectively.

He is currently a Postdoctoral Research Associate with the Center for Mechanics of Solids, Structures, and Materials, University of Texas at Austin, Austin, TX. His research interests include micro/nanosystems, micro/nanomechanics, and mechanics of polymers.

Dr. Zhu is a member of the American Society of Mechanical Engineers (ASME), Society for Experimental Mechanics (SEM), and Materials Research Society (MRS). He serves as a Reviewer for the *International Journal of Solids and Structures*, *Journal of Microelectromechanical Systems*, *International Journal of Fracture*, *Journal of Micromechanics & Microengineering*, and *Experimental Mechanics*. He received the Best Poster Award from the Gordon Conference on Thin Film & Small Scale Mechanical Behavior in 2006.



**Nicolaie Moldovan** received the Masters and Ph.D. degrees in physics from the University of Bucharest, Bucharest, Romania.

He was the head of the Microfabrication Laboratory, Romanian Institute for Microtechnology. In 1998–2002, he was with Argonne National Laboratory, where he developed micromachining techniques for new materials and applications such as microoptics, X-ray optics, microfluidics, and microelectromechanical systems. He is currently a Research Professor with the Department of Mechanical

Engineering, Northwestern University, Evanston, IL. His professional interests center on better understanding of fundamental laws governing phenomena at micro- and nanoscale.